crystals

MDPI

Article

Modification of TiO_2 Nanowire Arrays with Sn Doping as Photoanode for Highly Efficient Dye-Sensitized Solar Cells

Shiming Ni, Fengyun Guo *, Dongbo Wang *, Shujie Jiao, Jinzhong Wang, Yong Zhang, Bao Wang, Pu Feng and Liancheng Zhao

Department of Optoelectronic Information Science, School of Materials Science and Engineering, Harbin Institute of Technology, Harbin 150001, China; nishiming1989@163.com (S.N.); shujiejiao@gmail.com (S.J.); jinzhong_wang@hit.edu.cn (J.W.); Yongzhang@hit.edu.cn (Y.Z.); baowang@stu.hit.edu.cn (B.W.); 17S009003@stu.hit.edu.cn (P.F.); lczhao@hit.edu.cn (L.Z.)

* Correspondence: guowen@hit.edu.cn (F.G.); wangdongbo@hit.edu.cn (D.W.); Tel.: +86-138-4509-7528 (F.G.); +86-131-0166-0586 (D.W.)

Received: 31 January 2019; Accepted: 16 February 2019; Published: 21 February 2019

Abstract: The dye-sensitized solar cell (DSSC) is one candidate among the third-generation solar cells. The performance of most DSSCs based on TiO_2 photoanode was limited by the low electron mobility within TiO_2. To produce a much higher power conversion efficiency, Sn-doped TiO_2 nanowire arrays were successfully prepared using a simple hydrothermal process. It was found that Sn doping augments electron mobility well and raises the flat band potential to improve the performance of DSSCs. The power conversion efficiency (η) of a DSSC based on the reasonable Sn-doped TiO_2, N719 dye, platinized counter electrode and iodide/triiodide electrolyte reaches 8.75%. Furthermore, with an anatase TiO_2 light scattering layer, a DSSC based on the Sn-doped TiO_2 NWAs exhibits a remarkable power conversion efficiency of 9.43%, which is especially useful in weak light conditions.

Keywords: dye-sensitized solar cell; TiO_2 nanowires; Sn-doped; electron mobility; N719

1. Introduction

Replacing the badly polluting fossil energy with environment-friendly renewable energy sources is perhaps the best way to solve the global energy crisis. As well as various clean energy sources such as hydrogen, wind, geothermal and tidal energy, solar energy seems to be a good candidate to be the next generation energy source because the irradiation energy provided by the sun to the surface of the earth exceeds global energy consumption. Methods for converting solar energy into usable energy is therefore the most important research and development issue for researchers.

A solar cell based on photovoltaic (PV) technology is a way to convert solar energy into directly available electric energy [1,2]. Since the silicon-based solar cell was first designed [3], solar cells have been developing over several stages. Nevertheless, the application of the silicon-based solar cells (single or multi crystalline) is limited by complex preparation methods and high manufacturing costs. The remarkable invention of the dye-sensitized solar cell (DSSC) by Grätzel and his cooperators [4]—a photoelectrochemical cell—has drawn much attention due to low manufacturing cost, simple manufacturing process and being environmentally friendly [5]. Over the past two decades, the power conversion efficiency of the dye-sensitized solar cell has been low compared with the silicon-based solar cell, but the DSSC is still a considerable candidate for producing a much higher power conversion efficiency at a later time [6–11].

As a rule, DSSC is a sandwich structure composed of a photoanode covered with a monolayer of dye molecules on a semiconductor surface, electrolytes and a counter electrode [12]. Much endeavor has been focused on the design or modification of the novel dyes [13], the novel types of electrolyte [14] or counter electrodes [15]. The photoanode also plays a key role in the operation of the DSSC, therefore, it is crucial to develop new photoanodes to improve the power conversion efficiency of DSSC.

Numerous semiconductor materials have been investigated for use as photoanodes in DSSCs, such as TiO_2 [16], ZnO [17], SnO_2 [18], In_2O_3 [19]. Among these semiconductor materials, most researchers employed TiO_2 nanomaterials as the photoanode of DSSCs owing to its excellent physical and chemical properties such as having a suitable isoelectric point for dye absorption, proper energy band structure for charge injection from dye molecules, well passivity to photo corrosion [20–23], and appropriate electronic orbit for reducing probability of photogenerated charges recombination [24]. In a general way, tetragonal anatase and rutile TiO_2 are commonly applied in DSSCs, and rutile is the most stable crystalline phase of TiO_2. The relatively lower electron mobility of rutile TiO_2 leads to larger density of states near the conduction band minimum, which could provide additional efficient electron transfer channels to render much faster electron transfer in DSSCs based on rutile TiO_2 [25].

The photoanode needs the highest possible specific surface area for dye adsorption, a porous structure for complete electrolyte immersion and a fast charge mobility rate to minimize photogenerated charges loss [26]. In early research, TiO_2 nanoparticles (NPs) were usually used as the photoanode of DSSCs [4]. NPs can provide a very large surface area for dye adsorption due to large specific surface area, electron traps caused by massive amounts of grain boundaries still limit the further improvement of the performance of DSSCs [27–32]. Extensive efforts to overcome this disadvantage have been focused on the preparation of single-crystal one-dimensional (1D) nanostructures such as nanorods (NRs), nanowires (NWs), nanotubes (NTs) and nanobelts (NBs) [33–36]. Compared with NPs film, single-crystal 1D nanostructures could provide direct carrier transport pathways to the external circle, which would increase the charge carrier collection. There are fewer defects in single-crystal 1D nanostructures of high crystallization quality, which decrease the recombination of the photogenerated carriers in the photoanode [37,38]. Among these nanostructures, rutile TiO_2 nanowire arrays (NWAs) are considered because they maintain the advantages of one-dimensional nanomaterials, while the large specific surface area can load more dye molecules.

Low electron mobility hampers the application of rutile TiO_2 NWAs in DSSCs. Doping elements is a practical method for optimizing the TiO_2 NWAs. Doping elements could shift the flat-band potential, decrease the recombination rate of photogenerated carriers and increase the speed of electron transport, but the choice of doping elements is predominant for the performance of DSSCs. Various elements of doped TiO_2 nanostructures have been studied in DSSCs such as V [39,40], Cr [41,42], Mn [43], Fe [44], Cu [45], Zn [46–52]. However, DSSCs based on Sn-doped TiO_2 NWAs photoanodes have not been studied. Stannum (Sn) is a candidate for doping into the crystal lattice of rutile TiO_2. The crystal structure and lattice constant of Tin dioxide (SnO_2) are close to those of rutile TiO_2, so the doping would not introduce defects that would trap the photogenerated electrons. The electron mobility and band gap of SnO_2 is 100~200 $cm^2\ V^{-1}\ s^{-1}$ [53] and 3.8 eV, respectively, which are higher than those of rutile TiO_2 (0.1–1 $cm^2\ V^{-1}\ s^{-1}$ [54], 3.0 eV). It could be expected that doping Sn into rutile TiO_2 NWAs could well augment the electron mobility, thus decreasing the recombination possibility of photogenerated electrons at the interface of photoanode and electrolyte [55] Compared with TiO_2, the lower isoelectric point of SnO_2 limited the loading of acidic carboxyl dye molecules [56]. So, finding a suitable doping ratio of Sn is a crucial work.

In this paper, we prepared Sn-doped TiO_2 NWAs using a simple hydrothermal process and then assembled DSSCs based on these photoanodes with N719 dye, platinized counter electrode and iodide/triiodide electrolyte. It was found that Sn doping augments electron mobility well and raises the flat band potential to improve the performance of DSSC. Furthermore, with an anatase TiO_2 light scattering layer, DSSC based on the Sn-doped TiO_2 NWAs exhibits a remarkable power conversion efficiency of 9.43%.

2. Results and Discussion

The preparation of pure TiO_2 NWAs (TS0) and Sn-doped TiO_2 NWAs (TS1, TS2, TS3, TS4) is shown in the Supplementary Materials. First, we used inductively coupled plasma optical emission spectrometry to measure the ratio of Sn/Ti. With $SnCl_4$ increasing in reaction resolution, the ratio of Sn/Ti is about 5/95, 11/89, 15/85 and 21/79, respectively, consistent with the reaction resolution.

The crystalline structure and the lattice parameters were examined using X-ray diffraction (XRD, PANalytical B.V., Almelo, Holland) in the 2θ range of 30°~80°. XRD patterns of pure TiO_2 NWAs (TS0) and Sn-doped TiO_2 NWAs (TS1, TS2, TS3, TS4) are shown in Figure 1a. The only diffraction peak of TS0 was located at 62.72° which could be indexed to the rutile phase TiO_2 (JCPDS 21-1276) and the small half-peak width indicated single growth orientation and high crystallization quality. The (002) plane suggests that [001] orientation is the crystal preferential orientation of the hydrothermal method to prepare TiO_2 NWAs. No extra peaks could be explained by the uniformity of the Sn doping and the formation of the uniform solid solution. As the XRD pattern of the (002) peak was enlarged, it was noted that with the amount of Sn doping increasing, the position of the diffraction peak of TS1, TS2, TS3 and TS4 moved to a smaller angle, as shown in Figure 1b. The shift of the position of the diffraction peak means the augment of lattice parameters, which may be related to that the ionic radii of Ti ions (0.061 nm), is smaller than that of Sn ions (0.071 nm) [57].

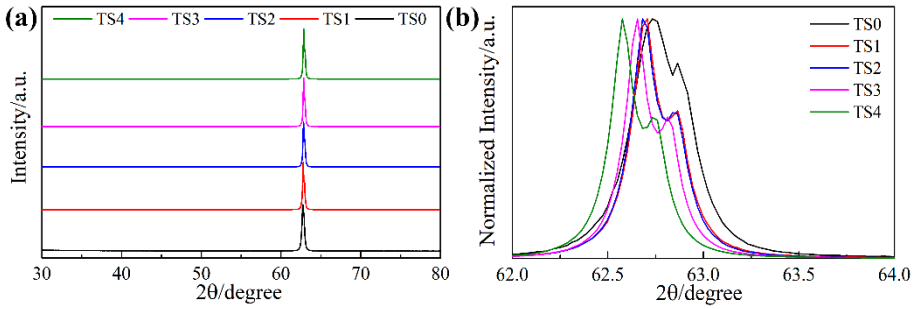

Figure 1. (**a**) X-Ray diffraction (XRD) patterns of pure TiO_2 NWAs (TS0) and Sn-doped TiO_2 NWAs (TS1, TS2, TS3, TS4), (**b**) enlarged XRD patterns of pure TiO_2 NWAs (TS0) and Sn-doped TiO_2 NWAs (TS1, TS2, TS3, TS4).

Raman spectroscopy (HORIBA Jobin Yvon, Pairs, France) was employed to further analyze the spatial uniformity and variation of bonds to characterize the effect of the Sn-doping in the TiO_2 NWs. Figure 2a shows the Raman spectra of samples TS0, TS1, TS2, TS3 and TS4 in the range of 100–800 cm^{-1}. For the pure rutile TiO_2 (sample TS0), four typical vibrational modes were perceived for rutile TiO_2 around 145 cm^{-1} (B_{1g}), 445 cm^{-1} (E_g), 610 cm^{-1} (A_{1g}), and 240 cm^{-1} for second-order effect (SOE) [58–60]. No peaks related to SnO_2 were detected, also indicating the uniformity of the Sn doping and the formation of the uniform solid solution. These typical vibrational modes were comprised of Ti-O bonds and the variation of lattice parameters resulted in the opposite moving of the O atoms in the adjacent O-Ti-O bonds [61]. Apparently, their positions moved to a lower wavenumber as the contents of Sn increased. As shown in Figure 2b, the red-shift of the B_{1g}, E_g and A_{1g} mode of samples TS1, TS2, TS3, TS4 suggested the more internal strains were caused by Sn-doping in the NWs and a smaller Hooke constant, indicating weaker Ti-O bond involvement and larger lattice parameters, consistent with the XRD results.

In order investigate the Sn-doped TiO_2 NWAs—a substitutional solid solution or interstitial solid solution—X-ray photoelectron spectroscopy (XPS, Thermo Fisher Scientific, Waltham, MA, USA) was used to analyze the bonding state of samples TS2. For the pure rutile TiO_2, the two characteristic peaks of the Ti 2p spectrum were located at 464.4 eV and 458.6 eV, which are related to Ti $2p_{1/2}$ and $2p_{3/2}$, respectively [62,63]. For the pure rutile SnO_2, the two characteristic peaks of the Sn 3d spectrum were located at 495.4 eV and 486.9 eV, which are related to $3d_{3/2}$ and $3d_{5/2}$, respectively [64,65]. As shown

in Figure 3a, the fully scanned XPS spectra confirmed that the existence of Ti, Sn, and O were detected in the nanowire. As shown in Figure 3b, the peak positions of two detected peaks in the spectrum of the Ti 2p showed a small positive shift of 0.1 eV toward higher binding energy compared to the pure rutile TiO_2. Meanwhile, the peak positions of the two detected peaks in the spectrum of the Sn 3d showed a small negative shift of 0.4 eV toward lower binding energy compared to the pure rutile TiO_2, as shown in Figure 3c. Considering that the electronegativity of Ti (1.54) is a little smaller than that of Sn (1.96) vs, the small shift of binding energy is ascribed to the presence of Sn metallic ions in TiO_2 lattice bringing about parts of electrons deviating from the Ti metallic ions [66–69]. The small shift of binding energy also confirms that the Sn replaces the Ti in the TiO_2 lattice but does not embed in the lattice gap. In other words, the Sn doping is also uniform at the atomic level, which was consistent with the XRD and Raman results. The O 1s spectrum of Sample TS3 can be deconvoluted to two peaks, as shown in Figure 3d. The binding energy of O-Ti is 529.36 eV, and the binding energy of O-Sn is about 530.8 eV. One peak of the O 1s spectrum located at 529.5 eV, which suggests the formation of a Sn-O-Ti linkage in the nanowire [70]. The peak located at 531.1 eV is assigned to oxygen vacancy and the surface-adsorbed H_2O [71–73].

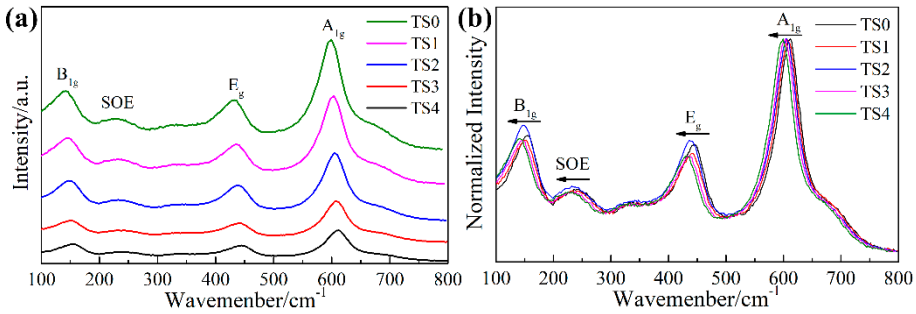

Figure 2. (**a**) Raman patterns of pure TiO2 NWAs (TS0) and Sn-doped TiO2 NWAs (TS1, TS2, TS3, TS4); (**b**) normalized Raman patterns of pure TiO2 NWAs (TS0) and Sn-doped TiO2 NWAs (TS1, TS2, TS3, TS4).

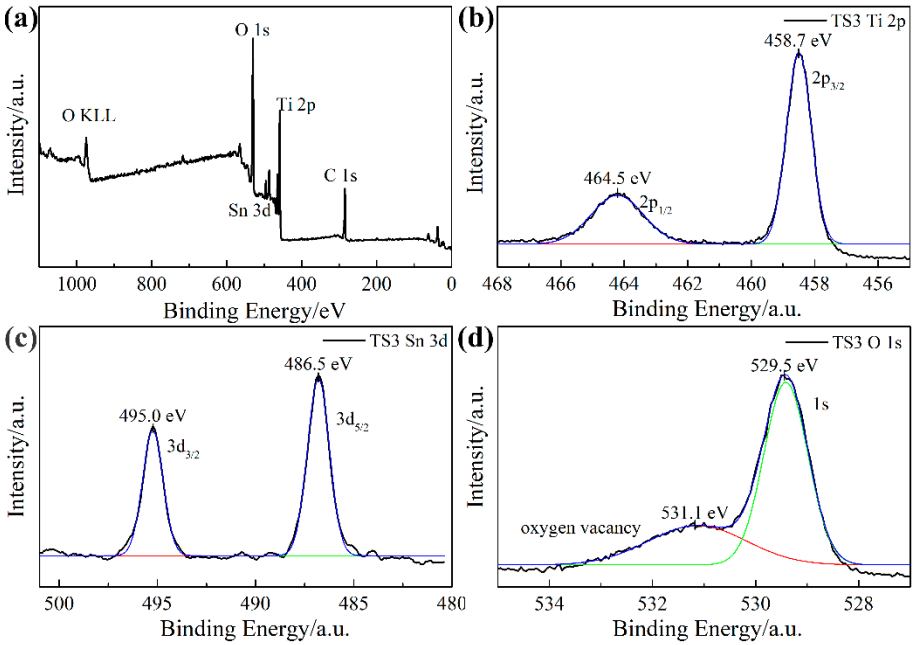

Figure 3. (**a**) X-ray photoelectron spectroscopy (XPS) patterns of Sn-doped TiO_2 NWAs (TS2), (**b**) Ti 2p peaks, (**c**) Sn 3d peaks, (**d**) O 1s peaks.

The microstructure and microtopography are of great significance for the performance of nanomaterials. The morphology of pure TiO_2 NWAs (TS0) and Sn-doped TiO_2 NWAs (TS1, T32, TS3, TS4) were examined using the field emission scanning electron microscopy (FESEM, JEOL, Akishima-shi, Tokyo, Japan). Figure 4a–e are the top-surface images of different samples, in which we can clearly observe highly uniform and ordered nanowires with square cross sections. The average square edge length of each nanowire is approximately 15 nm which means that the concentration of Sn in the reaction solution does not affect the cross sections of all samples. Figure 4f–j show cross-sectional images of different samples, indicating that the growth of nanowires is almost perpendicular to the FTO substrates. This result is consistent with the XRD result. Obviously, the thickness of the NWAs is affected by the concentration of Sn in the reaction solution. While the concentration of Sn in the reaction solution is low, the thicknesses of TS1 and TS2 are nearly the same as that of the pure TiO_2 NWAs (TS0, 30 μm); however, with the concentration of Sn in the reaction solution increasing, for TS3 and TS4, the thickness decreases to 26 and 20 μm, respectively. As we know, the deposition and dissolution of NWs are processes of dynamic equilibrium. Because the SnO_2 is more easily eroded by HCl, as the concentration of Sn in the reaction solution increases, the dissolution of NWs aggravates, leading to less thickness. Figures S1 and S2 depict the element-mapping characterization of the top-surface area and the cross section of the Sn-doped TiO_2 NWAs (TS2), indicating that Sn is homogeneously distributed in TiO_2 NWAs.

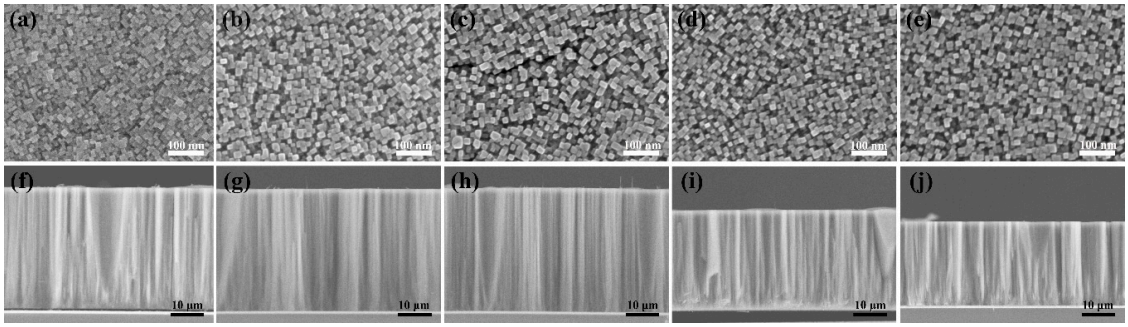

Figure 4. Morphological characterizations of pure TiO_2 NWAs (TS0) and Sn-doped TiO_2 NWAs (TS1, TS2, TS3, TS4): (**a**–**e**) top-surface field emission scanning electron microscopy (FESEM) image of TS0, TS1, TS2, TS3, TS4, respectively; and (**f**–**j**) cross-sectional FESEM image of TS0, TS1, TS2, TS3, TS4, respectively.

Transmission electron microscopy (TEM, JEOL, Akishima-shi, Tokyo, Japan) and high-resolution TEM (HRTEM, JEOL Akishima-shi, Tokyo, Japan) were used to examine more detailed data about the microstructures of the Sn-doped TiO_2 NWAs (sample TS2). As shown in Figure 5a, the structure of the Sn-doped TiO_2 NWAs is porous, which helps dye loading and electrolyte penetration which is beneficial for the improvement of DSSCs. The clear lattice fringes can be found in the HRTEM image, as shown in Figure 5b. The ~0.342 nm interplanar spacing of the Sn-doped TiO_2 NWAs is a little more than that of pure TiO_2 NWAs, suggesting the formation of the Sn-doped TiO_2 NWAs, consistent with above results. The distribution of Sn in nanowires (sample TS2) was investigated by TEM with an electron energy loss spectrometer (EELS). As shown in Figure S3, EELS elemental mappings also indicate that the Sn is uniformly distributed among entire TiO_2 NWs, indicating the formation of Sn doped TiO_2 NWAs.

The pure TiO_2 nanowire arrays and Sn-doped TiO_2 nanowire arrays with N719 dye platinized counter electrode and iodide/triiodide electrolyte were employed as photoanodes to prepare the DSSCs. The detailed methods are shown in the Supplementary Materials. Figure 6a shows the typical current density (J)−voltage (V) curves of the as-prepared DSSCs based on the pure TiO_2 NWAs and Sn-doped TiO_2 NWAs under simulated AM1.5G sunlight with 100 mW cm^{-2}, and the corresponding detailed DSSC parameters are listed in Table 1. The short-circuit photocurrent density (J_{sc}), open-circuit

voltage (V_{oc}), fill factor (FF) and power conversion efficiency (η) of the DSSC based on the pure TiO_2 NWAs (TS0) are 13.46 mA cm^{-2}, 748 mV, 0.741 and 7.46%, respectively. For DSSCs based on the Sn-doped TiO_2 NWAs (TS1, TS2, TS3, TS4) with an increasing doping amount of Sn, the J_{sc} augments from 14.28 to 15.84 mA cm^{-2} and then decreases to 8.73 mA cm^{-2}; meanwhile, the V_{oc} gradually increased. The increased V_{oc} is related to higher flat-band potentials, as shown in Figure S4 [74]. A maximum η of 8.72% was obtained for the DSSC based on TS2 Sn-doped TiO_2 NWAs photoanode, which may be mostly attributed to the largest J_{sc}.

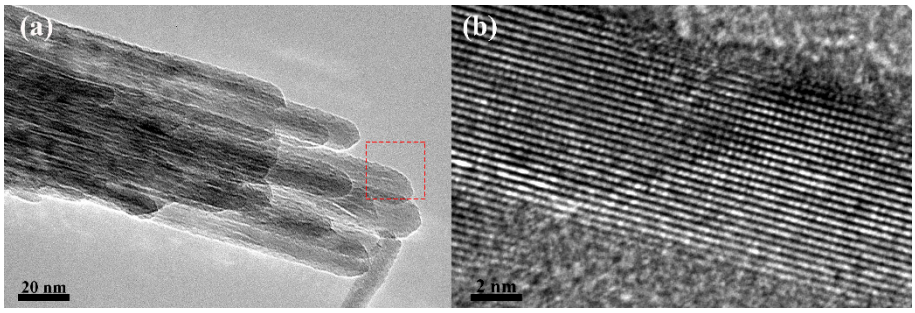

Figure 5. (**a**) Transmission electron microscopy (TEM) images and (**b**) High resolution transmission electron microscopy (HRTEM) image of Sn-doped TiO_2 NWAs (TS2).

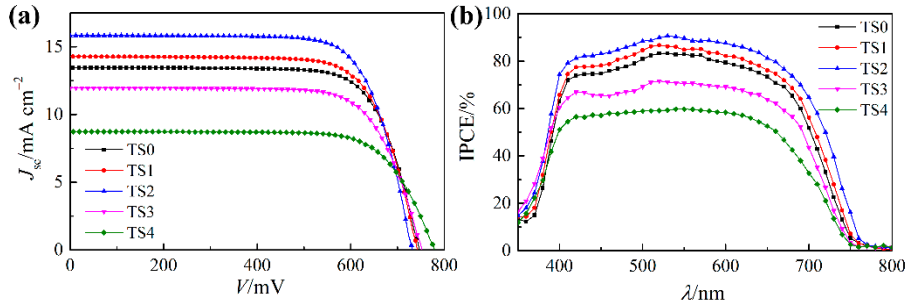

Figure 6. (a) *J*–*V* characteristics under an irradiance of 100 mW cm^{-2} simulated AM1.5G sunlight and (b) IPCE spectra of DSSC based on pure TiO_2 NWAs (TS0) and Sn-doped TiO_2 NWAs (TS1, TS2, TS3, TS4).

Table 1. Detailed data of *J*–*V* characteristics DSSC based on pure TiO_2 NWAs (TS0) and Sn-doped TiO_2 NWAs (TS1, TS2, TS3, TS4).

Sample	J_{sc} (mA cm^{-2})	V_{oc} (mV)	FF (%)	η (%)	Dye Loading (nmol cm^{-2})
TS0	13.46	748	0.741	7.46	390.4
TS1	14.28	750	0.738	7.90	382.7
TS2	15.84	755	0.732	8.75	375.4
TS3	11.96	760	0.776	7.05	325.2
TS4	8.73	763	0.782	5.21	288.6

To seek the cause of the J_{sc} changes, the incident photon-to-current conversion efficiency (IPCE) spectra of DSSCs based on the pure TiO_2 NWAs and Sn-doped TiO_2 NWAs was tested in the range of 350~800 nm. As shown in Figure 6b, the change trend of IPCE is consistent with that of J_{sc} of DSSCs. The IPCE of the DSSC with TS2 is higher than that of DSSC with other photoanodes (TS0, TS1, TS3) over the spectra ranging from 400~800 nm. Nevertheless, the IPCE enhanced with the increasing Sn amount over the spectra ranging from 350~400 nm. For the TS3 and TS4, the lower IPCE may be due to the smaller thickness which could not load enough dye molecule and higher flat-band potentials may inhibit injection of photoelectrons [74].

Compared with the DSSC based on pure TiO_2 NWAs, the enhancement in the IPCE for the DSSCs based on Sn-doped TiO_2 NWAs may be attributed to the light harvesting ability and photogenerated electron recombination at the interface of photoanode and electrolyte [75].

The light harvesting ability is related to the dye-uptake amounts and the light trapping by the photoanode. For the pure TiO_2 NWAs and Sn-doped TiO_2 NWAs, the dye-uptake amounts decreased from 390.4 to 288.6 nmol cm^{-2} as the doping amount of Sn increased, as shown in Table 1. The dye-uptake amount is relevant to the isoelectric points of photoanode. Considering the lower isoelectric point (IEP) of SnO_2 is lower than that of TiO_2 [76], the decrease of the dye-uptake amounts could be understood. As shown in Figure S5, compared to the isoelectric point of the pure TiO_2 NWAs, the presence of Sn in TiO_2 NWAs decreases the isoelectric point from 6.4 to 5.8, which would inhibit the attachment of dye molecules with acidic carboxyl groups [77]. The smaller thickness would also decrease the dye-uptake amounts.

To make certain the effect of the doping amount of Sn on the light trapping by the photoanode, UV-vis diffuse reflectance spectra measurement was carried out. The thickness of NWAs is so large that no light could pass through the nanowire arrays, in other words, the less reflection indicates more absorption. As shown in Figure S6a, the variation in the reflection of the pure TiO_2 NWAs (TS0) and Sn-doped TiO_2 NWAs (TS1, TS2, TS3) is regular. With the doping amount of Sn increasing, the absorption of samples is enhanced at a range of wavelengths from 300 to 400 nm. This result is consistent with the IPCE result. The reflection rate was normalized, as shown in Figure S6b, indicating absorbing edge blue shifting. The equation for calculating the optical forbidden bandwidth from the diffuse reflectance is shown in the supplementary information. As shown in Figure S6c, the optical forbidden bandwidth of samples (TS0, TS1, TS2, TS3) with the doping amount of Sn is estimated to be 2.97, 3.00, 3.01 and 3.02, respectively. The larger band gap is beneficial to increasing the light absorption range of DSSCs.

To make clear the effect of the Sn doping in TiO_2 NWAs on photogenerated electron recombination at the interface of photoanode and electrolyte, we measured the dark current of DSSCs based on the pure TiO_2 NWAs (TS0) and Sn-doped TiO_2 NWAs (TS1, TS2, TS3, TS4). As shown in Figure S7, the Sn could reduce the dark current of the DSSCs at a given potential, indicating that Sn doping in TiO_2 NWAs can inhibit the photogenerated electron recombination at the interface of the photoanode and electrolyte. The lower dark current is related to higher V_{oc}, which is consistent with the above results [78].

To understand how to affect the photogenerated electron recombination at the interface of the photoanode and electrolyte, the photoluminescence (PL) spectrum was used to test the separation of photogenerated electron–hole pairs [79]. Figure 7a shows the PL spectra of the pure TiO_2 NWAs (TS0) and Sn-doped TiO_2 NWAs (TS1, TS2, TS3, TS4). It is noted that the intensity of PL peaks notably decreases as the doping amount of Sn increases, indicating that Sn doping could accelerate the separation of photogenerated electron–hole pairs. This may be due to the Sn doping enhancing the electron mobility of TiO_2 NWAs. To further analyze charge transfer kinetics in these DSSCs, electrochemical impedance spectroscopy (EIS) is carried out under 750 mV bias in dark conditions, as shown in the inset of Figure S8. All obtained curves show two arcs in low frequency and middle frequency regions. According to previous research, the enlarged low-frequency arc implies the charge transfer resistance of the photoanode, as shown in Figure S8 [80]. Through the fitting with Z-view, the resistance of the electrode could be calculated as shown in Table S1. As the doping amount of Sn increases, the charge transfer resistance gradually decreases, which certifies that the Sn doping can effectively improve charge transfer performance. We further utilized the transient photoelectric decay technique to find out the effect of the electron lifetime (τ_{tpd}) on the doping amount of Sn in the DSSCs based on the pure TiO_2 NWAs (TS0) and Sn-doped TiO_2 NWAs (TS1, TS2, TS3, TS4). As displayed in Figure 7b, the τ_{tpd} in DSSCs based on the Sn-doped TiO_2 (TS1, TS2, TS3, TS4) are non-negligibly higher than that of DSSC based on the pure TiO_2 NWAs (TS0) at a certain extracted charge. With the doping amount of Sn increasing, the τ_{tpd} augments, which is identical to the variation trend of the dark current.

Consistent with the PL results, the higher τ_{tpd} is mainly due to the Sn doping enhancing electron mobility [81–83], manifesting the noticeable suppression of the photogenerated electron recombination at the interface of the photoanode and electrolyte which contributes to higher IPCE and J_{sc} as well as V_{oc}.

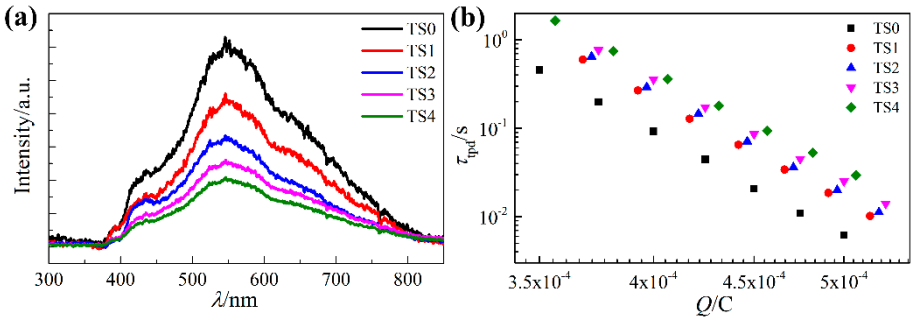

Figure 7. (**a**) Photoluminescence (PL) spectra of the pure TiO_2 NWAs (TS0) and Sn-doped TiO_2 NWAs (TS1, TS2, TS3, TS4), (**b**) Plots of lifetime of photoinjected electrons in the DSSCs based on the pure TiO_2 NWAs (TS0) and Sn-doped TiO_2 NWAs (TS1, TS2, TS3, TS4) as a function of charge.

Additional light scattering layer on the photoanode could effectively improve the performance of DSSC [80]. An anatase TiO_2 particles (WERO-4, Dyesol) layer with 5 μm thickness was used as a light scattering layer on the Sn-doped TiO_2 NWAs (TS2) by stencil printing, which was applied as a photoanode to prepared DSSC. As displayed in Figure 8, under a simulated AM1.5G sunlight irradiance of 100 mW cm^{-2}, as-prepared DSSC shows a remarkable η of 9.26% with J_{sc} of 17.28 mA cm^{-2}, V_{oc} of 735 mV, and FF of 0.729 which is a considerably high-power conversion efficiency for DSSCs. Moreover, the inset of Figure 8 showed the IPCE spectrum of this DSSC. The enhancement of IPCE is attributed to the efficient light harvesting due to the light-scattering layer of larger particles [84]. The power conversion efficiency of weak light also attracted the attention of researchers [85], so we measured the DSSC parameters under irradiation with different light intensities, and detailed data are listed in Table 2. Under an irradiation with 20.29 mW cm^{-2} light intensity, this DSSC reaches a remarkable power conversion efficiency of 9.43%.

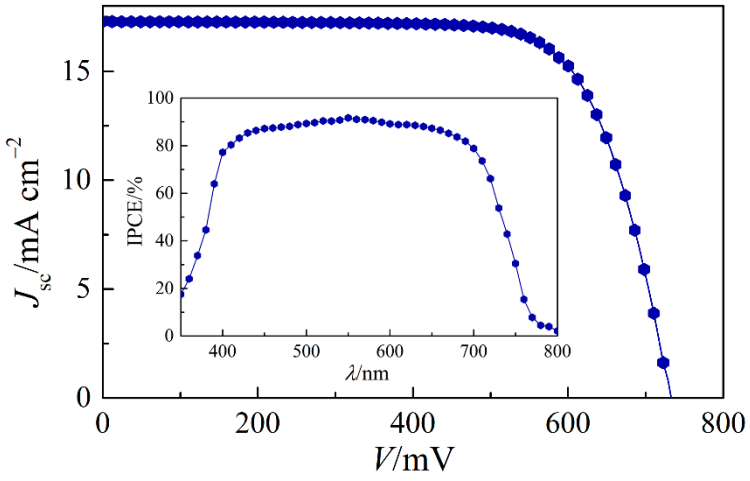

Figure 8. *J*–*V* characteristics of the cells based the DSSC based on the Sn-doped TiO_2 NWAs (TS2) with a light scattering layer under an irradiance of 100 mW cm^{-2} simulated AM1.5G sunlight. The inset is its IPCE spectrum.

Table 2. Detailed photovoltaic parameters of the DSSC based on the Sn-doped TiO_2 NWAs (TS2) with a light scattering layer under different incident light intensities.

P_{in} (mW cm^{-2})	J_{sc} (mA cm^{-2})	V_{oc} (mV)	FF	η (%)
100	17.28	735	0.729	9.26
63.63	11.39	708	0.733	9.29
50.33	9.28	684	0.741	9.35
20.29	3.85	664	0.749	9.43

3. Conclusions

We have successfully produced Sn-doped TiO_2 NWAs using simple hydrothermal methods and have analyzed their performance as a photoanode in DSSCs. The prepared Sn-doped is 30 μm length with a Square section of 15 nm average square edge length. XRD, Raman and XPS results confirmed the success of Sn doping. It is found that Sn doping augments electron mobility well and raises the flat band potential to improve the performance of DSSC. The power conversion efficiency (η) of DSSC based on the reasonable Sn-doped TiO_2, N719 dye, platinized counter electrode and iodide/triiodide electrolyte reaches 8.75%. Furthermore, with an anatase TiO_2 light scattering layer, DSSC based on the Sn-doped TiO_2 NWAs exhibits a remarkable power conversion efficiency of 9.43%, especially useful in the weak light conditions.

Supplementary Materials: The following are available online at http://www.mdpi.com/2073-4352/9/2/113/s1, Experimental method, Figure S1: EDS elemental mapping images of cross section of Sn-doped TiO_2 NWAs (TS2), Figure S2: EDS elemental mapping images of top surface of Sn-doped TiO_2 NWAs (TS2), Figure S3: (a) the tip region of Sn-doped TiO_2 NWAs (TS2). Corresponding EELS elemental mapping images for b) Sn, c) Ti, and d) O, respectively, Figure S4: Mott-Schottky plots of the pure TiO_2 NWAs (TS0) and Sn-doped TiO_2 NWAs (TS1, TS2, TS3, TS4), Figure S5: The pH-dependent zeta-potential of the pure TiO_2 NWAs (TS0) and Sn-doped TiO_2 NWAs (TS1, TS2, TS3, TS4)., Figure S6: (a) The UV-vis diffusive reflectance spectra of the pure TiO_2 NWAs (TS0) and Sn-doped TiO_2 NWAs (TS1, TS2, TS3), (b) normalized UV-vis diffusive reflectance spectra and (c) the plots of transforming the Kubelka–Munk function versus the energy of light, Figure S7: Dark current density–voltage of DSSCs based on the pure TiO_2 NWAs (TS0) and Sn-doped TiO_2 NWAs (TS1, TS2, TS3, TS4); Figure S8: The enlarged low-frequency arc and full scale (inset graph) Nyquist plots of the DSSCs based on the pure TiO_2 NWAs (TS0) and Sn-doped TiO_2 NWAs (TS1, TS2, TS3, TS4) measured under 750 mV bias in the dark condition; Table S1: Detailed simulative values of the charge transfer resistance from EIS spectra.

Author Contributions: F.G. and D.W. designed the experiments; S.N. and B.W. performed the experiments; S.N., Y.Z., J.W. and S.J. analyzed the data; Y.Z., J.W. and S.J. contributed analysis tools; S.N. and D.W. wrote the paper, L.Z. coordinated the overall work.

Funding: This research was funded by the National Natural Science Foundation of China (Grant No. 51502061) and (Grant No. 61605036).

Conflicts of Interest: The authors declare no conflict of interest.

References

1. Goetzberger, A.; Hebling, C.; Schock, H.W. Photovoltaic Materials, History, Status and Outlook. *Mater. Sci. Eng. R* **2003**, *40*, 1–46. [CrossRef]
2. Polman, A.; Knight, M.; Garnett, E.C.; Ehrler, B.; Sinke, W.C. Photovoltaic Materials: Present Efficiencies and Future Challenges. *Science* **2016**, *352*, aad4424. [CrossRef]
3. Chapin, D.M.; Fuller, C.S.; Pearson, G.L. A New Silicon p-n Junction Photocell for Converting Solar Radiation into Electrical Power. *J. Appl. Phys.* **1954**, *25*, 676–677. [CrossRef]
4. O'Regan, B.; Grätzel, M. A Low-cost, High-efficiency Solar Cell Based on Dye-sensitized Colloidal TiO_2 Films. *Nature* **1991**, *353*, 737–740. [CrossRef]
5. Fakharuddin, A.; Jose, R.; Brown, T.M.; Fabregat-Santiago, F.; Bisquert, J. A Perspective on the Production of Dye-sensitized Solar Modules. *Energy Environ. Sci.* **2014**, *7*, 3952. [CrossRef]
6. Hagfeldt, A.; Boschloo, G.; Sun, L.; Kloo, L.; Pettersson, H. Dye-sensitized Solar Cells. *Chem. Rev.* **2010**, *110*, 6595–6663. [CrossRef]

7. Snaith, H.J.; Schmidt-Mende, L. Advances in Liquid-electrolyte and Solid-state Dye-sensitized Solar Cells. *Adv. Mater.* **2007**, *19*, 3187–3200. [CrossRef]
8. Cuce, E.; Young, C.-H.; Riffat, S.B. Thermal performance investigation of heat insulation solar glass: A comparative experimental study. *Energy Build.* **2015**, *86*, 595–600. [CrossRef]
9. Cuce, E.; Riffat, S.B.; Young, C.-H. Thermal insulation, power generation, lighting and energy saving performance of heat insulation solar glass as a curtain wall application in Taiwan: A comparative experimental study. *Energ. Convers. Manag.* **2015**, *96*, 31–38. [CrossRef]
10. Kong, L.; Liu, G.; Gong, J.; Hu, Q.; Dera, P.; Zhang, D.; Liu, Z.; Yang, W.; Zhu, K.; Tang, Y.; et al. Simultaneous band-gap narrowing and carrier-lifetime prolongation of organic-inorganic trihalide perovskites. *Proc. Natl. Acad. Sci. USA* **2016**, *113*, 8910–8915. [CrossRef]
11. Nogueira, A.F.; Longo, C.; De Paoli, M.-A. Polymers in dye sensitized solar cells: Overview and perspectives. *Coord. Chem. Rev.* **2004**, *248*, 1455–1468. [CrossRef]
12. Huang, Y.; Wu, H.; Yu, Q.; Wang, J.; Yu, C.; Wang, J.; Gao, S.; Jiao, S.; Zhang, X.; Wang, P. Single-Layer TiO_2 Film Composed of Mesoporous Spheres for High-Efficiency and Stable Dye-Sensitized Solar Cells. *ACS Sustain. Chem. Eng.* **2018**, *6*, 3411–3418. [CrossRef]
13. Yu, Q.; Zhou, D.; Shi, Y.; Si, X.; Wang, Y.; Wang, P. Stable and efficient dye-sensitized solar cells: Photophysical and electrical characterizations. *Energy Environ. Sci.* **2010**, *3*, 1722–1725. [CrossRef]
14. Zhou, D.; Yu, Q.; Cai, N.; Bai, Y.; Wang, Y.; Wang, P. Efficient organic dye-sensitized thin-film solar cells based on the tris(1,10-phenanthroline) cobalt (II/III) redox shuttle. *Energy Environ. Sci.* **2011**, *4*, 2030–2034. [CrossRef]
15. He, B.; Meng, X.; Tang, Q. Low-Cost Counter Electrodes From CoPt Alloys For Efficient DyeSensitized Solar Cells. *ACS Appl. Mater. Interfaces* **2014**, *6*, 4812–4818. [CrossRef]
16. Yun, J.H.; Wang, L.; Amal, R.; Ng, Y.H. One-Dimensional TiO_2 Nanostructured Photoanodes: From Dye-Sensitised Solar Cells to Perovskite Solar Cells. *Energies* **2016**, *9*, 1030. [CrossRef]
17. Zhang, Q.; Dandeneau, C.S.; Zhou, X.; Cao, G. ZnO Nanostructures for Dye-Sensitized Solar Cells. *Adv. Mater.* **2009**, *21*, 4087–4108. [CrossRef]
18. Fukai, Y.; Kondo, Y.; Mori, S.; Suzuki, E. Highly Efficient Dye-Sensitized SnO_2 Solar Cells Having Sufficient Electron Diffusion Length. *Electrochem. Commun.* **2007**, *9*, 1439–1443. [CrossRef]
19. Mahalingam, S.; Abdullah, H. Electron Transport Study of Indium Oxide as Photoanode in DSSCs: A Review. *Renew. Sustain. Energy Rev.* **2016**, *63*, 245–255. [CrossRef]
20. Wang, X.; Li, Z.; Shi, J.; Yu, Y. One-Dimensional Titanium Dioxide Nanomaterials: Nanowires, Nanorods, and Nanobelts. *Chem. Rev.* **2014**, *114*, 9346–9384. [CrossRef]
21. Leung, D.; Fu, X.; Wang, C.; Ni, M.; Leung, M.; Wang, X.; Fu, X. Hydrogen Production over Titania-Based Photocatalysts. *ChemSusChem* **2010**, *3*, 681–694. [CrossRef] [PubMed]
22. Liu, G.; Kong, L.; Guo, P.; Stoumpos, C.C.; Hu, Q.; Liu, Z.; Cai, Z.; Gosztola, D.J.; Mao, H.; Kanatzidis, M.G.; et al. Two Regimes of Bandgap Red Shift and Partial Ambient Retention in Pressure-Treated Two-Dimensional Perovskites. *ACS Energy Lett.* **2017**, *2*, 2518–2524. [CrossRef]
23. Liu, G.; Gong, J.; Kong, L.; Schaller, R.D.; Hu, Q.; Liu, Z.; Yan, S.; Yang, W.; Stoumpos, C.C.; Kanatzidis, M.G.; et al. Isothermal pressure-derived metastable states in 2D hybrid perovskites showing enduring bandgap narrowing. *Proc. Natl. Acad. Sci. USA* **2018**, *115*, 8076–8081. [CrossRef] [PubMed]
24. Jose, R.; Thavasi, V.; Ramakrishna, S. Metal oxides for dye-sensitized solar cells. *J. Am. Ceram. Soc.* **2009**, *92*, 289–301. [CrossRef]
25. Wei, H.; Luo, J.; Li, S.; Wang, L. Revealing the Origin of Fast Electron Transfer in TiO_2-based Dye-Sensitized Solar Cells. *J. Am. Chem. Soc.* **2016**, *138*, 8165–8174. [CrossRef] [PubMed]
26. Roslan, N.; Ya'acob, M.E.; Radzi, M.A.M.; Hashimoto, Y.; Jamaludin, D.; Chen, G. Dye Sensitized Solar Cell (DSSC) greenhouse shading: New insights for solar radiation manipulation. *Renew. Sustain. Energy Rev.* **2018**, *92*, 171–186. [CrossRef]
27. Oekermann, T.; Zhang, D.; Yoshida, T.; Minoura, H. Electron Transport and Back Reaction in Nanocrystalline TiO_2 Films Prepared by Hydrothermal Crystallization. *J. Phys. Chem. B* **2004**, *108*, 2227–2235. [CrossRef]
28. Villanueva-Cab, J.; Wang, H.; Oskam, G.; Peter, L.M. Electron Diffusion and Back Reaction in Dye-Sensitized Solar Cells: The Effect of Nonlinear Recombination Kinetics. *J. Phys. Chem. Lett.* **2010**, *1*, 748–751. [CrossRef]

29. Fisher, A.C.; Peter, L.M.; Ponomarev, E.A.; Walker, A.B.; Wijayantha, K.G.U. Intensity Dependence of the Back Reaction and Transport of Electrons in Dye-Sensitized Nanocrystalline TiO_2 Solar Cells. *J. Phys. Chem. B* **2000**, *104*, 949–958. [CrossRef]
30. Nelson, J. Continuous-time random-walk model of electron transport in nanocrystalline TiO_2 electrodes. *Phys. Rev. B* **1999**, *59*, 15374. [CrossRef]
31. Kang, S.H.; Choi, S.H.; Kang, M.S.; Kim, J.Y.; Kim, H.S.; Hyeon, T.; Sung, Y.E. Nanorod-Based Dye-Sensitized Solar Cells with Improved Charge Collection Efficiency. *Adv. Mater.* **2008**, *20*, 54–58. [CrossRef]
32. Lee, B.H.; Song, M.Y.; Jang, S.-Y.; Jo, S.M.; Kwak, S.-Y.; Kim, D.Y. Charge Transport Characteristics of High Efficiency Dye-Sensitized Solar Cells Based on Electrospun TiO_2 Nanorod Photoelectrodes. *J. Phys. Chem. C* **2009**, *113*, 21453–21457. [CrossRef]
33. Zhou, Z.J.; Fan, J.Q.; Wang, X.; Zhou, W.H.; Du, Z.L.; Wu, S.X. Effect of Highly Ordered Single-Crystalline TiO_2 Nanowire Length on the Photovoltaic Performance of Dye-Sensitized Solar Cells. *ACS Appl. Mater. Interfaces* **2011**, *3*, 4349–4353. [CrossRef] [PubMed]
34. Yang, L.; Leung, W.W. Application of a Bilayer TiO_2 Nanofiber Photoanode for Optimization of Dye-Sensitized Solar Cells. *Adv. Mater.* **2011**, *23*, 4559–4562. [CrossRef] [PubMed]
35. Wang, Z.; Wang, H.; Liu, B.; Qiu, W.; Zhang, J.; Ran, S.; Huang, H.; Xu, J.; Han, H.; Chen, D.; et al. Transferable and Flexible Nanorod-Assembled TiO_2 Cloths for Dye-Sensitized Solar Cells, Photodetectors, and Photocatalysts. *ACS Nano* **2011**, *5*, 8412–8419. [CrossRef] [PubMed]
36. Sun, P.; Zhang, X.; Liu, X.; Wang, L.; Wang, C.; Yang, J.; Liu, Y. Growth of Single-Crystalline Rutile TiO_2 Nanowire Array on Titanate Nanosheet Film for Dye-Sensitized Solar Cells. *J. Mater. Chem.* **2012**, *22*, 6389–6393. [CrossRef]
37. Xie, J.L.; Guo, C.X.; Li, C.M. Construction of One-Dimensional Nanostructures on Graphene for Efficient Energy Conversion and Storage. *Energy Environ. Sci.* **2014**, *7*, 2559–2579. [CrossRef]
38. Weng, B.; Liu, S.; Tang, Z.-R.; Xu, Y.-J. One-Dimensional Nanostructure Based Materials for Versatile Photocatalytic Applications. *RSC Adv.* **2014**, *4*, 12685–12700. [CrossRef]
39. Liu, Z.; Li, Y.; Liu, C.; Ya, J.; Lei, E.; Zhao, W.; Zhao, D.; An, L. TiO_2 Photoanode Structure with Gradations in V Concentration for Dye-Sensitized Solar Cells. *ACS Appl. Mater. Interfaces* **2011**, *3*, 1721–1725. [CrossRef]
40. Liu, J.; Duan, Y.; Zhou, X.; Lin, Y. Influence of V_B Group Doped TiO_2 on Photovoltaic Performance of Dye-Sensitized Solar Cells. *Appl. Surf. Sci.* **2013**, *277*, 231–236. [CrossRef]
41. Xie, Y.; Huang, N.; You, S.; Liu, Y.; Sebo, B.; Liang, L.; Fang, X.; Liu, W.; Guo, S.; Zhao, X.-Z. Improved Performance of Dye-Sensitized Solar Cells by Trace Amount Cr-doped TiO_2 Photoelectrodes. *J. Power Sources* **2013**, *224*, 168–173. [CrossRef]
42. Kim, C.; Kim, K.S.; Kim, H.Y.; Han, Y.S. Modification of a TiO_2 Photoanode by Using Cr-doped TiO_2 with an Influence on the Photovoltaic Efficiency of a Dye-sensitized Solar Cell. *J. Mater. Chem.* **2008**, *18*, 5809–5814. [CrossRef]
43. Shalan, A.; Rashad, M. Incorporation of $Mn2^+$ and Co^{2+} to TiO_2 nanoparticles and the performance of dye-sensitized solar cells. *Appl. Surf. Sci.* **2013**, *283*, 975–981. [CrossRef]
44. Liau, L.C.-K.; Lin, C.-C. Fabrication and characterization of Fe^{3+}-doped titania semiconductor electrodes with p-n homojunction devices. *Appl. Surf. Sci.* **2007**, *253*, 8798–8801. [CrossRef]
45. Wijayarathna, T.R.C.K.; Aponsu, G.M.L.P.; Ariyasinghe, Y.P.Y.P.; Premalal, E.V.A.; Kumara, G.K.R.; Tennakone, K. A high efficiency indoline-sensitized solar cell based on a nanocrystalline TiO_2 surface doped with copper. *Nanotechnology* **2008**, *19*, 485703. [CrossRef] [PubMed]
46. Wang, K.-P.; Teng, H. Zinc-doping in TiO_2 films to enhance electron transport in dye-sensitized solar cells under low-intensity illumination. *Phys. Chem. Chem. Phys.* **2009**, *11*, 9489–9496. [CrossRef] [PubMed]
47. Zhang, Y.; Wang, L.; Liu, B.; Zhai, J.; Fan, H.; Wang, D.; Lin, Y.; Xie, T. Synthesis of Zn-doped TiO_2 microspheres with enhanced photovoltaic performance and application for dye-sensitized solar cells. *Electrochim. Acta* **2011**, *56*, 6517–6523. [CrossRef]
48. Zhang, X.; Wang, S.-T.; Wang, Z.-S. Effect of metal-doping in TiO_2 on fill factor of dye-sensitized solar cells. *Appl. Phys. Lett.* **2011**, *99*, 113503. [CrossRef]
49. Zhu, F.; Zhang, P.; Wu, X.; Fu, L.; Zhang, J.; Xu, D. The Origin of Higher Open-Circuit Voltage in Zn-Doped TiO_2 Nanoparticle-Based Dye-Sensitized Solar Cells. *ChemPhysChem* **2012**, *13*, 3731–3737. [CrossRef]
50. Zhu, G.; Cheng, Z.; Lv, T.; Pan, L.; Zhao, Q.; Sun, Z. Zn-doped Nanocrystalline TiO_2 Films for CdS Quantum Dot Sensitized Solar Cells. *Nanoscale* **2010**, *2*, 1229–1232. [CrossRef]

51. Niaki, A.H.G.; Bakhshayesh, A.M.; Mohammadi, M.R. Double-Layer Dye-Sensitized Solar Cells Based on Zn-doped TiO_2 Transparent and Light Scattering Layers: Improving Electron Injection and Light Scattering Effect. *Sol. Energy* **2014**, *103*, 210–222. [CrossRef]
52. Ali, Z.; Park, K.H.; Shakir, I.; Kang, D.J. Ultrathin Conformal Coating and Zn Doping in Nanocrystalline Mesoporous TiO_2 Micron-Sized Beads for Highly Efficient Dye Sensitized Solar Cells. *Electrochim. Acta* **2015**, *161*, 329–334. [CrossRef]
53. Qian, J.; Liu, P.; Xiao, Y.; Jiang, Y.; Cao, Y.; Ai, X.; Yang, H. TiO_2-Coated Multilayered SnO_2 Hollow Microspheres for Dye-sensitized Solar Cells. *Adv. Mater.* **2009**, *21*, 3663–3667. [CrossRef]
54. Breckenridge, R.G.; Hosler, W.R. Electrical Properties of Titanium Dioxide Semiconductors. *Phys. Rev.* **1953**, *91*, 793–802. [CrossRef]
55. Ramasamy, E.; Lee, J. Ordered Mesoporous SnO_2-Based Photoanodes for High-Performance Dye-Sensitized Solar Cells. *J. Phys. Chem. C* **2010**, *114*, 22032–22037. [CrossRef]
56. Parks, G.A. The Isoelectric Points of Solid Oxides, Solid Hydroxides, and Aqueous Hydroxo Complex Systems. *Chem. Rev.* **1965**, *65*, 177–198. [CrossRef]
57. Zhang, J.; Peng, W.; Chen, Z.; Chen, H.; Han, L. Energy Band Tunable $Ti_xSn_{1-x}O_2$ Photoanode for Efficient non-TiO_2 Type Dye Sensitized Solar Cells. *J. Mater. Chem. A* **2013**, *1*, 8453–8463. [CrossRef]
58. Gervais, F.; Piriou, B. Temperature Dependence of Transverseand Longitudinal-Optic Modes in TiO_2 (Rutile). *Phys. Rev. B* **1974**, *10*, 1642–1654. [CrossRef]
59. Swamy, V.; Muddle, B.C.; Dai, Q. Size-dependent modifications of the Raman spectrum of rutile TiO_2. *Appl. Phys. Lett.* **2006**, *89*, 163118. [CrossRef]
60. Lan, T.; Tang, X.; Fultz, B. Phonon Anharmonicity of Rutile TiO_2 Studied by Raman Spectrometry and Molecular Dynamics Simulations. *Phys. Rev. B* **2012**, *85*, 094305. [CrossRef]
61. Zhang, Y.; Harris, C.X.; Wallenmeyer, P.; Murowchick, J.; Chen, X. Asymmetric Lattice Vibrational Characteristics of Rutile TiO_2 as Revealed by Laser Power Dependent Raman Spectroscopy. *J. Phys. Chem. C* **2013**, *117*, 24015–24022. [CrossRef]
62. Sanjines, R.; Tang, H.; Berger, H.; Gozzo, F.; Margaritondo, G.; Levy, F. Electronic structure of anatase TiO_2 oxide. *J. Appl. Phys.* **1994**, *75*, 2945–2951. [CrossRef]
63. Aas, N.; Pringle, T.; Bowker, M. Adsorption and Decomposition of Methanol on TiO2, SrTiO3 and SrO. *J. Chem. Soc. Faraday Trans.* **1994**, *90*, 1015–1022. [CrossRef]
64. Jing, L.; Fu, H.; Wang, B.; Wang, D.; Xin, B.; Li, S.; Sun, J. Effects of Sn Dopant on the Photoinduced Charge Property and Photocatalytic Activity of TiO_2 Nanoparticles. *Appl. Catal. B* **2006**, *62*, 282–291. [CrossRef]
65. Li, J.; Zeng, H.C. Hollowing Sn-doped TiO_2 Nanospheres via Ostwald Ripening. *J. Am. Chem. Soc.* **2007**, *129*, 15839–15847. [CrossRef]
66. Barr, T.L. Recent Advances in X-ray Photoelectron Spectroscopy Studies of Oxides. *J. Vac. Sci. Technol. A* **1991**, *9*, 1793–1805. [CrossRef]
67. Barr, T.L.; Lishka, M.A.; Chen, L.M.; Mohsenian, M. XPS Valence Band Study of Zeolites and Related Systems. 1. General Chemistry and Structure. *J. Am. Chem. Soc.* **1988**, *110*, 7962–7975. [CrossRef]
68. Teo, S.H.; Zeng, H.C. Surface and Textural Properties of Network-Modified Silica as a Function of Transition Metal Dopant Zirconium. *J. Phys. Chem. B* **2001**, *105*, 9093–9100. [CrossRef]
69. Zhu, J.; Chen, F.; Zhang, J.; Chen, H.; Anpo, M. Fe^{3+}-TiO_2 photocatalysts prepared by combining sol-gel method with hydrothermal treatment and their characterization. *J. Photochem. Photobiol. A Chem.* **2006**, *180*, 196–204. [CrossRef]
70. Chen, D.; Gao, L. Novel Synthesis of Well-Dispersed Crystalline SnO_2 Nanoparticles by Water-in-Oil Microemulsion-Assisted Hydrothermal Process. *J. Colloid Interface Sci.* **2004**, *279*, 137–142. [CrossRef]
71. Xu, R.; Zeng, H.C. Self-Generation of Tiered Surfactant Superstructures for One-Pot Synthesis of Co_3O_4 Nanocubes and Their Close- and Non-Close-Packed Organizations. *Langmuir* **2004**, *20*, 9780–9790. [CrossRef] [PubMed]
72. Chang, Y.; Lye, M.L.; Zeng, H.C. Large-Scale Synthesis of High-Quality Ultralong Copper Nanowires. *Langmuir* **2005**, *21*, 3746–3748. [CrossRef] [PubMed]
73. Li, J.; Zeng, H.C. Preparation of Monodisperse Au/TiO_2 Nanocatalysts via Self-Assembly. *Chem. Mater.* **2006**, *18*, 4270–4277. [CrossRef]

74. Feng, X.; Shankar, K.; Paulose, M.; Grimes, G.A. Tantalum-Doped Titanium Dioxide Nanowire Arrays for Dye-Sensitized Solar Cells with High Open-Circuit Voltage. *Angew. Chem. Int. Ed.* **2009**, *48*, 8095–8098. [CrossRef] [PubMed]
75. Snaith, H.J.; Ducati, C. SnO_2-Based Dye-Sensitized Hybrid Solar Cells Exhibiting Near Unity Absorbed Photon-to-Electron Conversion Efficiency. *Nano Lett.* **2010**, *10*, 1259–1265. [CrossRef] [PubMed]
76. Khan, M.Z.H.; Al-Mamun, M.R.; Halder, P.K.; Aziz, M.A. Performance improvement of modified dye-sensitized solar cells. *Renew. Sust. Energ. Rev.* **2017**, *71*, 602–617. [CrossRef]
77. Kay, A.; Grätzel, M. Dye-Sensitized Core-Shell Nanocrystals: Improved Efficiency of Mesoporous Tin Oxide Electrodes Coated with a Thin Layer of an Insulating Oxide. *Chem. Mater.* **2002**, *14*, 2930–2935. [CrossRef]
78. Huang, Y.; Yu, Q.; Wang, J.; Wang, J.; Yu, C.; Abdalla, J.T.; Zeng, Z.; Jiao, S.; Wang, D.; Gao, S. Plasmon-Enhanced Self-Powered UV Photodetectors Assembled by Incorporating Ag@ SiO_2 Core-Shell Nanoparticles into TiO_2 Nanocube Photoanodes. *ACS Sustain. Chem. Eng.* **2017**, *6*, 438–446. [CrossRef]
79. Ni, S.; Guo, F.; Wang, D.; Liu, G.; Xu, Z.; Kong, L.; Wang, J.; Jiao, S.; Zhang, Y.; Yu, Q.; et al. Effect of MgO Surface Modification on the TiO_2 Nanowires Electrode for Self-Powered UV Photodetectors. *ACS Sustain. Chem. Eng.* **2018**, *6*, 7265–7272. [CrossRef]
80. Dou, X.; Sabba, D.; Mathews, N.; Wong, L.H.; Lam, Y.M.; Mhaisalkar, S. Hydrothermal Synthesis of High Electron Mobility Zn-doped SnO_2 Nanoflowers as Photoanode Material for Efficient Dye-Sensitized Solar Cells. *Chem. Mater.* **2011**, *23*, 3938–3945. [CrossRef]
81. Kim, C.W.; Suh, S.P.; Choi, M.J.; Kang, Y.S.; Kang, Y.S. Fabrication of $SrTiO_3$-TiO_2 heterojunction photoanode with enlarged pore diameter for dye-sensitized solar cells. *J. Mater. Chem. A* **2013**, *1*, 11820–11827. [CrossRef]
82. Li, Z.; Zhou, Y.; Yu, T.; Liu, J.; Zou, Z. Unique Zn-doped SnO_2 nano-echinus with excellent electron transport and light harvesting properties as photoanode materials for high performance dye-sensitized solar cell. *CrystEngComm* **2012**, *14*, 6462–6468. [CrossRef]
83. Bisquert, J.; Fabregat-Santiago, F.; Mora-Seró, I.; Garcia-Belmonte, G.; Giménez, S. Electron Lifetime in Dye-Sensitized Solar Cells: Theory and Interpretation of Measurements. *J. Phys. Chem. C* **2009**, *113*, 17278–17290. [CrossRef]
84. Wang, Z.S.; Kawauchi, H.; Kashima, T.; Arakawa, H. Significant Influence of TiO_2 Photoelectrode Morphology on the Energy Conversion Efficiency of N719 Dye-Sensitized Solar Cell. *Coord. Chem. Rev.* **2004**, *248*, 1381–1389. [CrossRef]
85. Grätzel, M. Recent Advances in Sensitized Mesoscopic Solar Cells. *Acc. Chem. Res.* **2009**, *42*, 1788–1798. [CrossRef] [PubMed]